ACS OMEGA

Open Access

http://pubs.acs.org/journal/acsodf

Article

Pyridyl Aroyl Hydrazone-Based Metal Complexes Showing a Ligand-Centered Metal-Assisted Pathway for Electrocatalytic Hydrogen Evolution

Bharath M,[†] Gargee Roy,[†] Aryya Ghosh,* Munmun Ghosh,* and Deepak Asthana*

Cite This: *ACS Omega* 2025, 10, 3511−3519

Read Online

ACCESS | Metrics & More | Article Recommendations | Supporting Information

ABSTRACT: In the past few decades, the concern over the excessive use of fossil fuels and consequent environmental damage has triggered the search for cleaner and renewable energy resources. This has led to the consideration of hydrogen as our future fuel. It can be produced from various sources, and if used as fuel, it generates only water as a byproduct. Electrocatalytic reduction of protons ($2H^+ + 2e^- \rightarrow H_2$) is one of the available methods for producing hydrogen gas at large scales. Currently, the most efficient electrocatalysts are Pt-based complexes. In order to make the entire process more cost-effective, it has become necessary to find electrocatalysts that are derived from earth-abundant metals such as Ni, Zn, Fe, etc. Herein, we have demonstrated the electrocatalytic hydrogen evolution reaction (HER) catalyzed by pyridyl aroyl hydrazone ligand (HL)-based metal complexes (M = Fe, Co, Ni, Cu, and Zn). Rate calculations using controlled potential electrolysis revealed the optimal overall catalytic performance of NiL_2 among the investigated complexes. For NiL_2, a maximum turnover frequency of 7040 s^{-1} with a 0.42 V overpotential was obtained when triethylamine hydrochloride was used as a proton source. Both experimental and density functional theory (DFT) calculations suggested a ligand-centered metal-assisted catalysis pathway for NiL_2 in the presence of triethylammonium chloride.

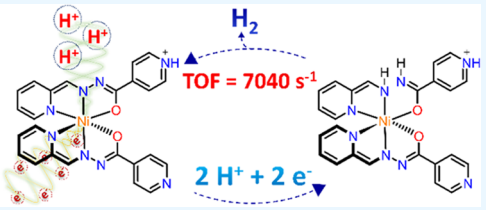

1. INTRODUCTION

The constant rise in energy demands, depleting fossil fuel reserves, and alarming environmental changes has kindled the need for carbon neutral energy systems.[1,2] In this context, hydrogen can be considered the most reliable resource.[3,4] However, most methods of hydrogen production are not carbon neutral.[4−6] The electrocatalytic hydrogen production might provide a benign method for mass production of H_2. As the effectiveness of the electrocatalytic method depends on the efficiency of the applied catalyst, extensive efforts have been made to find the most suitable catalytic systems. To date, platinum-based electrocatalysts have been widely applied, but the increased cost along with low availability limits their usage to a great extent.[7−15] A likely solution to this could be the development of earth-abundant metal-based catalysts or metal-free catalysts.[16−27]

Usually, metal-based catalysts follow a metal-centered pathway; however, in some cases, the alternative ligand-centered pathway is also possible.[24,28−32] Recent studies by Grapperhaus and co-workers have suggested that harmony between the metal and ligand redox properties greatly influences the catalytic performance of metal complexes.[24,30,33,34] Herein, we report a ligand-centered reactivity in a Ni complex in the presence of a weaker acid, triethylammonium chloride (TEA).

We prepared pyridyl aroyl hydrazone-based metal complexes ML_2 (M = Fe, Co, Ni, Cu, and Zn; Scheme 1) and tested their ability toward electrocatalytic HER activity. In our investigation of these complexes, we revealed the optimal overall catalytic performance by NiL_2. From the mechanistic analysis of NiL_2, we observed that ligand protonation was favored over metal hydride formation. Similar experimental results were obtained for Fe, Co, Cu, and Zn complexes as well.

Scheme 1. Molecular Structure of Ligand (HL) and Metal Complexes (ML_2)

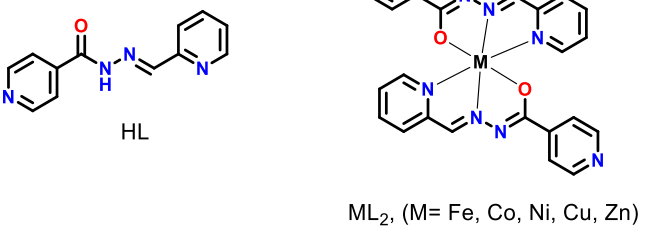

Received: August 22, 2024
Revised: December 6, 2024
Accepted: December 12, 2024
Published: January 17, 2025

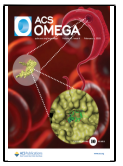

2. RESULTS AND DISCUSSION

2.1. Synthesis and Characterization. The synthesis of the ligand (**HL**) and complexes **1**−**5** (ML_2) was performed by following procedures reported elsewhere.[35,36] The ligand and complexes were characterized by various analytical methods, including ^{1}H NMR, ESI-MS, FT-IR, UV−vis, elemental analysis (C, H, and N), and powder X-ray diffraction (PXRD) analyses (Figures S1−S10). The exact synthesis and purification details are provided in the Supporting Information (see pages 1−7). The microcrystalline samples for all of the complexes were obtained by the slow evaporation method. To ensure the structure of formed complexes, wherever possible, the PXRD patterns of freshly synthesized complexes were compared with the simulated PXRD patterns generated using the single-crystal X-ray analysis data from the literature (Figure S10). An absolute match in PXRD patterns was observed for CuL_2 and NiL_2. Simulated PXRD patterns of CuL_2 were used to find a match with the experimental powder patterns for FeL_2 and ZnL_2 complexes.

2.2. Electrochemical Properties. Electrochemical properties of metal complexes were analyzed in 0.1 M TBAF/DMF (tetrabutylammonium tetrafluoroborate in dimethylformamide) solution at 100 mV/s. The cyclic voltammogram (CV) of FeL_2 and CoL_2 displayed two reversible redox events, whereas CuL_2 and NiL_2 displayed one reversible and one irreversible reduction event. For ZnL_2, two quasi-reversible redox events at −1.83 and −2.1 V versus Fc/Fc^+ were observed (Figure S11). CVs for all of the complexes were found to match well with earlier reports.[36] The half-wave potentials are listed in Table 1. The reversible redox events in the case of FeL_2 can be both metal- and ligand-centered redox processes.[36] However, the reversible redox events in NiL_2, CoL_2, and CuL_2 are attributed to metal-based $M^{2+/+}$ redox processes, and the quasi-reversible process is attributed to ligand-based reductions. To understand if the redox events were diffusion-controlled, CV measurements were performed at variable scan rates. A linear relationship between peak currents and the square root of the scan rate was observed, which suggested the nature of redox events to be diffusion-controlled (Figure S12).[37] Diffusion coefficient values were determined for ML_2 complexes using the Randles−Ševčík equation (see the Supporting Information for more details).

Table 1. Reference-Calibrated Half-Wave Potentials for the Reversible Redox Event ($E_{1/2}$), Cathodic Peak Potential (E_{pc}), and Half-Wave Potential of the First Catalytic Wave (E_{cat})[a]

complex	$E_{1/2}$ (V) vs Fc^+/Fc	E_{pc} (V) vs Fc^+/Fc	E_{cat} (V) vs Fc^+/Fc
FeL_2	−1.59, −2.19		−1.5
CoL_2	−1.41	−2.04	−1.31
NiL_2	−1.77	−2.17	−1.54
CuL_2	−0.94	−2.18	−1.60
ZnL_2		−1.83, −2.10	−1.66

[a]Catalyst concentration: 0.6 mM in 0.1 M TBAF/DMF, substrate concentration: 3.6 mM TEA, WE: glassy carbon electrode (diameter: 2 mm), RE: $Ag/AgNO_3$, CE: Pt coil (scan rate:100 mV/s), and internal standard: Fc^+/Fc couple.

2.3. Hydrogen Evolution Reaction (HER). The electrocatalytic hydrogen evolution reaction by employing the prepared complexes (**1**−**5**) as catalysts was evaluated in DMF using triethylammonium chloride ($HNEt_3Cl$, pK_a = 9.2 in DMF, henceforth referred to as TEA) as the proton source (Figure 1). Our choice of TEA as a proton source is based on the fact that it does not undergo homoconjugation in the operating media.[37] As a control study, triethylammonium tetrafluoroborate ($TEABF_4$) was also used as a proton source. No noticeable changes in catalytic behavior were observed in the presence of $TEABF_4$, which indicated no anion interference in the catalysis (Figure S20a,c). The successive addition of TEA to ML_2 (0.6 mM) in 0.1 M TBAF/DMF generated two catalytic waves. For all of the complexes, the addition of TEA first initiated a single catalytic wave that gets saturated with further addition of acid (except for ZnL_2, Figure S13). This is followed by the subsequent generation of the second catalytic wave (Figures S18−S21). Notably, distinct characteristics were displayed by the complexes for the initial catalytic wave (Figures S13−S17). In the case of ZnL_2, CoL_2 (Figure S14), and NiL_2 (Figure S15), a precatalytic wave was observed, and for CuL_2, the catalytic wave was formed at a more negative potential than the $Cu^{II/I}$ standard reduction potential (Figure S16). Also, a consistent anodic shift in reduction potential from −0.94 to −0.65 V was observed for CuL_2. For copper complexes, similar findings have been earlier reported by Grapperhaus and co-workers.[30] The initial catalytic wave for FeL_2 was developed on top of the $Fe^{II/I}$ redox couple (Figure S17).

The onset potential for the catalytic wave shifted anodically from $M^{II/I}$ reduction potential with a shift value of 150 mV for NiL_2, 100 mV for FeL_2 and CoL_2, and 250 mV for ZnL_2 with 1.0 equiv of TEA. This anodic shift in potential is suspected to be due to the formation of protonated species. To confirm this, ultraviolet−visible (UV−vis) absorption spectra in the presence and absence of TEA were recorded in DMF. FeL_2 displayed two characteristic bands at 358 and 666 nm in the absence of TEA (Figure S9). In the presence of 1−5 equiv of TEA, the band at 358 nm diminished drastically and the band at 666 nm disappeared along with a concomitant appearance of a new band at 298 nm. For CoL_2, a characteristic band was observed at 367 nm in the absence of TEA. With the addition of 1−20 equiv of TEA, the band at 367 nm diminished without complete quenching. The concomitant appearance of a new band at 298 nm was observed in CoL_2 also. A similar observation was observed in the case of CuL_2, with addition of 1−15 equiv of TEA, the characteristic band at 384 nm diminished with the concurrent appearance of a new band at 300 nm. ZnL_2 displayed an absorption band at 380 nm, which was quenched completely with 1−5 equiv addition of TEA. In this case, a new band was observed at 300 nm. Unlike other complexes, the absorption spectrum of NiL_2 does not show any change upon the addition of TEA (see Figure 1).

For complexes FeL_2, CoL_2, CuL_2, and ZnL_2, a considerable shift in half-wave potential and a noticeable change in absorption spectra in the presence of TEA suggest that protonation takes place prior to an electron transfer. The fact that TEA was unable to protonate NiL_2 in its neutral state suggests an electron transfer step to initiate the catalytic cycle for NiL_2. Thus, the precatalytic wave observed in the case of NiL_2 could be a proton-coupled electron transfer (PCET) step, suggesting an EC process (E corresponds to electrochemical reduction and C denotes a protonation step), where the initial step is a one-electron reduction of $Ni^{II/I}$.[38] UV−vis. absorption experiments were repeated for NiL_2 with a stronger acid, such as trifluoroacetic acid (TFA, pK_a ∼4.2 in DMF). In the presence of 1−5 equiv of TFA, the band at 390 nm quenched

https://doi.org/10.1021/acsomega.4c07748
ACS Omega 2025, 10, 3511−3519

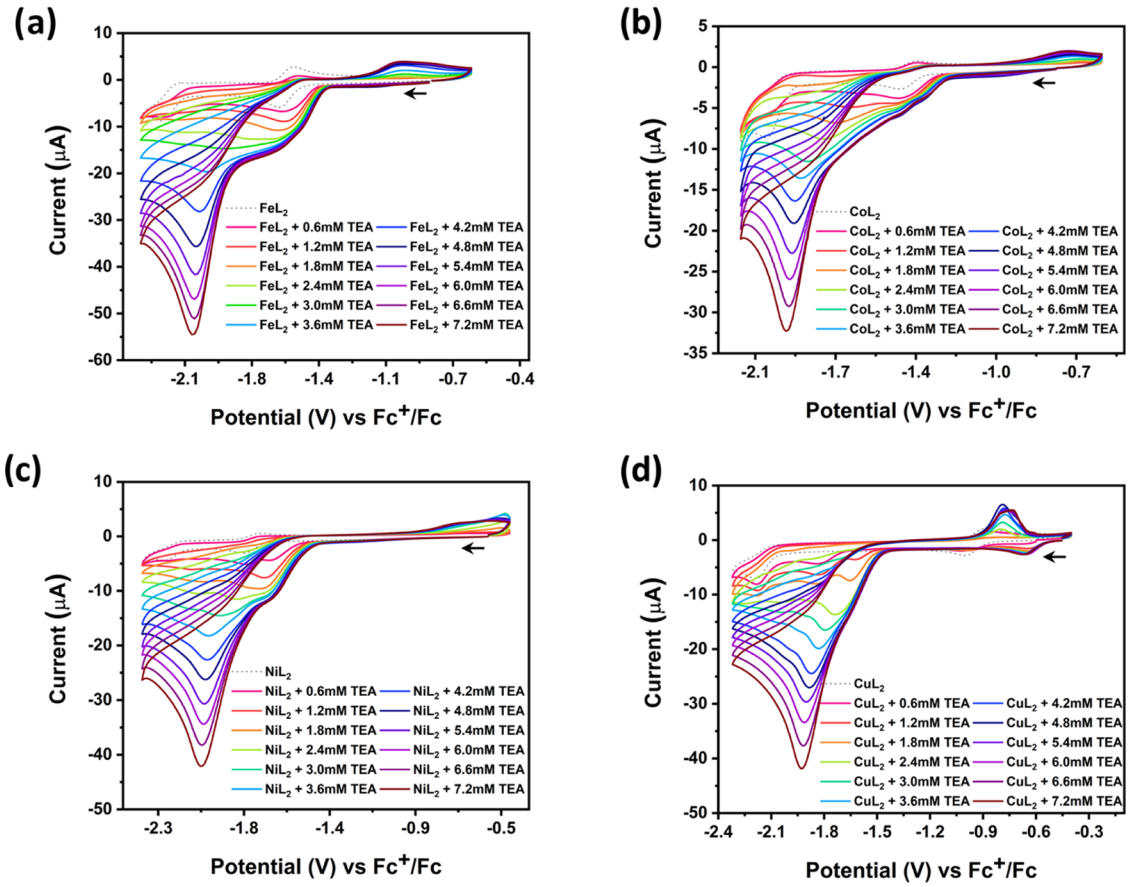

Figure 1. Cyclic voltammograms for electrocatalytic HER of the complexes (a) FeL_2, (b) CoL_2, (c) NiL_2, and (d) CuL_2 in a 0.1 M TBAF/DMF solution using TEA as a proton source.

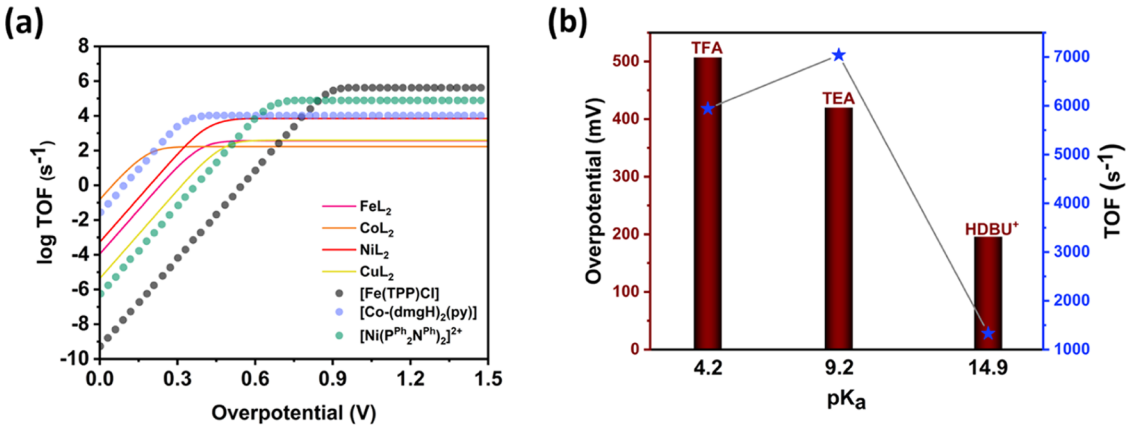

Figure 2. (a) Tafel plot of ML_2 in the presence of TEA with previously reported H_2 evolving catalysts: [Fe(TPP)Cl], [Co-$(dmgH)_2$(py)], and $[Ni(P_2^{Ph}N^{Ph})_2]^{2+}$.[25−27,37] Reprinted (adapted in part) with permission from refs 25,27, and 37. Copyright 1996, 2005, and 2020 American Chemical Society. Reprinted (adapted in part) with permission from ref 26. Copyright 2011, The American Association for the Advancement of Science (AAAS). (b) Comparison of overpotential (represented by the red column) and TOF (represented by the blue star) for NiL_2 in the presence of TFA (pK_a = 4.2), TEA (pK_a = 9.2), and $HDBU^+$ (pK_a = 14.9) in DMF (rate was calculated from CPC with 0.1 M acid concentration and normalized to 1.0 M acid concentration).

completely with the concurrent appearance of a new band at 300 nm (Figure S22b). This strongly suggests the formation of protonated NiL_2. This observation is in good agreement with the electrochemical studies of NiL_2 in the presence of TFA (Figure S22a). The onset potential of the catalytic wave was ∼400 mV anodic to the $Ni^{II/I}$ redox couple with 3 mM TFA addition.

For the calculation of rate constants for the rate-determining step, controlled potential electrolysis (CPC) experiments (3 h) were performed. Among the complexes, NiL_2 showed the maximum catalytic rate of 7.04×10^3 M^{-1} s^{-1} from the CPC experiment (Table S4). Therefore, further experimental and theoretical analyses were performed for NiL_2. Electrocatalytic studies of NiL_2 were extended to different proton sources for understanding the effect of pK_a in deciding the rate and

https://doi.org/10.1021/acsomega.4c07748
ACS Omega 2025, 10, 3511−3519

mechanism for HER. As suspected, NiL_2 displayed distinct electrochemical behavior in different acids, implying varying catalytic routes for different pK_a conditions (Figures S20, S22, and S23). Rate constants were derived for each condition using CPC experiments, and they were compared with previous results (Figure S31). Though we expected an inverse relation between the turnover frequency (TOF) and acid strength, this was not followed when TFA was used as a proton source (Table S5). We presume that TFA has an adverse effect on the stability of the complex.[39] Lowest overpotential and TOF values were shown by $HDBU^+$ (1,8-diazabicyclo[5.4.0]undec-7-ene). Thus, TEA was found to be the better proton source for NiL_2 among the three (Figure 2b). Even though NiL_2 showed stability in the presence of TEA during the voltammetric experiments, this was not the case observed during electrolysis experiments. Thus, electrolysis experiments were limited to 3 h, and the rate constant calculations were performed for this time (Figure S32).

For calculating faradaic efficiency (FE) and turnover number (TON), separate time-dependent electrolysis experiments with NiL_2 (0.6 mM) in DMF with 45 mM TEA were conducted. An FE value of 93% with a TON of 29 was obtained.[24] Figure 2a shows the "catalytic Tafel plot" for ML_2 in comparison with those of previously reported catalysts. To construct this plot, we used the rate constants extracted from the electrolysis experiments. Among the ML_2 complexes, maximum catalytic rates were shown by NiL_2 with an overpotential requirement of 420 mV. Noticeably, the catalytic rates for NiL_2 were comparable with those of some of the best state-of-the-art catalysts (Figure 2a).[25−27] In terms of overpotential, NiL_2 turns out to be a better catalyst than the earlier reported complexes such as $[Ni(P_2^{Ph}N^{Ph})_2]^{2+}$ and Fe(TPP) system.[26,27] Complex NiL_2 fails to match with the catalytic rates shown by the existing state-of-the-art Ni, Co, and Fe electrocatalysts. However, when compared with the recently reported Ni complexes (Table S8), NiL_2 is found to be either better or equivalent in overall electrocatalytic activity. In addition, it could be seen that CoL_2 exhibited overpotential values comparable with the well-known cobaloxime[25] electrocatalyst.

The stability of NiL_2 as an HER electrocatalyst was examined by performing CPC experiments for 24 h using a mercury pool working electrode (Figure S29). Throughout the electrolysis, the TOF remained consistent, with no signs of catalyst decomposition. The identity of the gaseous product as H_2 was confirmed from the GC-TCD (gas chromatography using a thermal conductivity detector) analysis of the gas collected from the headspace of the electrolysis cell (Figure S30). A control experiment was performed under the same conditions in the absence of NiL_2, producing a significantly less amount of hydrogen. Bulk electrolysis using a mercury pool electrode ruled out the possibility of any electrodeposited Ni nanoparticle that can act as an HER catalyst, as they would amalgamate within the mercury pool electrode.[40] Additionally, UV−vis absorption spectra recorded before and after electrolysis experiments at potentials near the first catalytic wave showed no signs of catalyst decomposition.

2.4. Control Experiments—Rinse Test. A series of control experiments were performed to identify the nature of the active catalyst. First, a set of chronoamperometric (CA) experiments were conducted at potentials varying from −1.5 to −2.2 V (Figure S26).[41] From the CA experiments conducted at −1.5 to −1.8 V, a current decay was observed after the initial current spike, which is suspected to be due to substrate depletion. But at higher negative potentials, beyond −1.9 V, the current decay was slower, which could be due to the formation of an electroactive film at higher negative potentials. This was further confirmed from rinse test experiments performed for electrodes procured from CV experiments until −1.9 V (potential where the first catalytic wave ends). First, a freshly polished glassy carbon (GC) electrode was used to perform CV for a single scan in a solution containing a catalyst and a proton source. The electrode was rinsed with an electrolyte solution, and CV scans were performed in a solution containing only the substrate. The experiment is then repeated for 10 scans and 50 scans.[42] We could not observe any catalytic response, indicating the absence of film formation until −1.9 V (Figure S27). Additionally, bulk electrolysis experiments performed using a mercury pool working electrode at −1.7 V showed similar catalytic rates to those calculated using a GC plate electrode (Figure S29). The above-mentioned observations clearly indicate that NiL_2 in solution is responsible for the initial catalytic wave observed.

Later, a rinse test was performed for single scans until −2.3 V, which suggested the formation of an active film, and the catalytic current observed for the film was almost double that of NiL_2 in solution, confirming the activity of the film (Figure S28).[24] As film formation was evident at higher negative potentials, we refrained from any analysis for rate calculation and mechanistic investigation beyond the potential for the first catalytic event.[43]

2.5. Mechanistic Analysis. Theoretical calculations have been proven to be quite useful in finding the observed/proposed catalytic mechanisms and in determining the thermodynamic and kinetic parameters involved in a catalytic cycle. In order to gain insights into possible mechanistic steps, DFT calculations were performed. The geometry optimization of possible intermediates and frequency calculations were done employing B3LYP (hybrid GGA) and BP86 (GGA) functionals with 6-31G and 6-311G basis sets using ORCA.[44] The structure of the starting catalyst $[NiL_2]^0$ was optimized using both levels of theory in the gas and solution phases using the CPCM solvation model for DMF. The bond length from the optimized geometry was compared to the corresponding crystal structure.

The average deviation from experimental bond lengths obtained for BP86 is 0.91%, and for B3LYP, it is 1.1% (Table S6). The better fit BP86/6-311G method was used for further calculations in gas and solvent phases.[45]

The spin state for the neutral Ni(II) complex is a d^8 system with a triplet ground state (S = 1). Reduction of $[NiL_2]^0$ by one electron yields a doublet electronic state (S = 1/2), best described as the reduced Ni(I) complex with a total charge of −1. From the spin density plots of $[NiL_2]^0$ and $[NiL_2]^{-1}$, it was evident that upon reduction, the electron density over the metal center increases along with partial delocalization across the ligand, suggesting a metal-centered reduction (Figure 4). This assignment of the first reduction as metal-centered is consistent with the experimental results. A theoretical standard reduction potential value for the first reduction event of NiL_2 was obtained using the Born−Haber cycle. The reduction potentials are reported versus the ferrocene/ferrocenium couple to match the experimental results. The first reduction event of $[NiL_2]^0$ assigned as $Ni^{II/I}$ reduction was computed to be −1.701 V (with respect to the computed Fc/Fc^+ couple, 5.001 V). This value is in good agreement with the experimental value of 1.772 V for the $Ni^{II/I}$ reduction. A

https://doi.org/10.1021/acsomega.4c07748
ACS Omega 2025, 10, 3511−3519

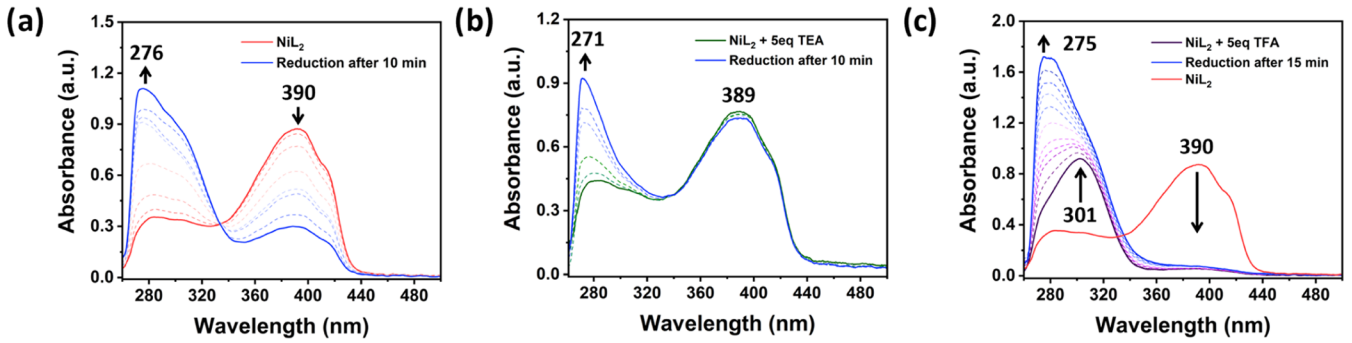

Figure 3. Spectral changes upon electrochemical reduction of NiL_2 (a) at an applied potential of −0.9 V, (b) at an applied potential of −1.1 V in the presence of 3.0 mM TEA, and (c) at an applied potential of −0.9 V in the presence of 3.0 mM TFA (red trace—NiL_2, blue trace—NiL_2 after reduction, green trace—NiL_2 + TEA, and violet trace—NiL_2 + TFA).

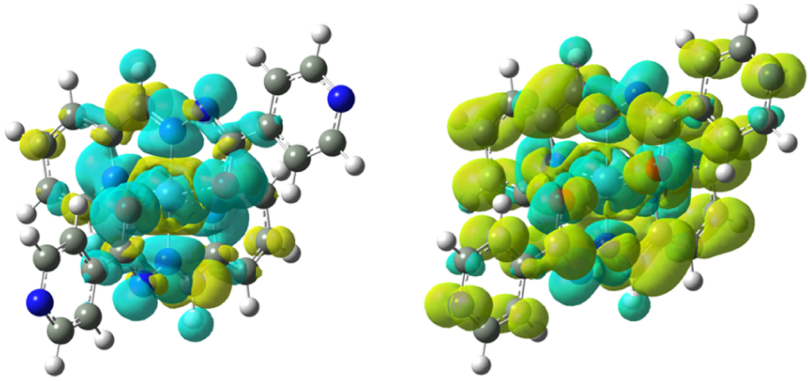

Figure 4. Electron spin density plot for $[NiL_2]^0$ (left, isovalue 0.003) and $[NiL_2]^{-1}$ (right, isovalue 0.003).

summary of the calculation is provided in the Supporting Information (Section 4.9).[46]

The favorability of protonation prior to the reduction was checked by optimizing the structures of $[NiL_2H]^1$ followed by frequency calculations. From the calculations, it was evident that the protonation of $[NiL_2]^0$ prior to the reduction step is less favored. Despite that, the lowest energetic pathway for the formation of $[NiL_2H]^0$ is not the EC pathway (E corresponds to electron transfer, and C corresponds to a chemical step). Rather, a much more stable $[NiL_2H]^0$ intermediate was formed through a CE pathway (see Figure 5). These computed results can be clearly correlated to the UV−vis acid titration experiments of $[NiL_2]^0$. In the presence of weaker acids such as $HDBU^+$ and TEA, no characteristic change in UV−vis spectra was observed upon their addition. This indicated their inability to protonate $[NiL_2]^0$ prior to its reduction. Rather, a stronger acid such as TFA could initiate the energetically favorable protonation step prior to reduction and form a $[NiL_2H]^0$ intermediate following a CE pathway. To understand the electronic changes associated with $[NiL_2]^0$ upon reduction in the presence and absence of a proton source, UV−vis spectroelectrochemical (UV−vis SEC) experiments were performed. Figure 3a shows the changes in UV−vis absorption spectra upon reduction of $[NiL_2]^0$ in the absence of a proton source. Reduction at −0.9 V suppressed the characteristic band at 390 nm with a concomitant appearance of a new band at 276 nm (blue trace). This observation signified the charge transfer from the metal to the ligand network upon reduction, as observed from spin density plots in Figure 4. UV−vis SEC experiments in the presence of TEA and TFA showed totally different absorption spectra for $[NiL_2]^0$. Prior to electrolysis, absorption spectra in the presence of TEA showed no characteristic change (Figure 3c, green trace), but this was not the case in the presence of TFA. The characteristic band at 390 nm diminished with a concomitant appearance of a new band at 301 nm (Figure 3c, violet trace). Upon electrolysis, this band further shifted to 275 nm, suggesting a metal-to-ligand charge transfer. From this, it is confirmed that TFA protonates $[NiL_2]^0$ prior to its reduction, and the band originating at 301 nm corresponds to the band of the protonated derivative $[NiL_2H]^1$. Upon electrolysis, the protonated derivative is reduced, and the band at 301 nm shifts to 275 nm, implying a metal-to-ligand charge transfer. This was further supported by the spin density plots of different $[NiL_2H]^0$ intermediates (Figure S34). For all those intermediates, electron density was majorly delocalized over the ligand framework. In the presence of TEA, electrolysis of $[NiL_2]^0$ resulted in the formation of a new band at 271 nm, keeping the characteristic band at 390 nm intact. The above-mentioned observations suggest that the reduction of $[NiL_2]^0$ results in delocalization of electron density across the ligand in both cases, namely, the presence and absence of the proton source. These inferences can be clearly visualized from the spin density plots of all these intermediates, suggesting a good agreement between experimental and computed results.

The first protonation of $[NiL_2]^{-1}$ was examined by considering various probable sites (Figure S33), including Ni, N_2 (coordinated pyridine), N_4 (imino), N_6 (amidic), N_8 (uncoordinated pyridine), and O_2 (amidic). Each of these states was evaluated in the doublet ground states ($S = 1/2$). Frequency calculations favor the first protonation on the non-coordinating pyridinyl ring nitrogen N_8. All other protonation

https://doi.org/10.1021/acsomega.4c07748
ACS Omega 2025, 10, 3511−3519

sites were disfavored by at least 6.55 kcal/mol. Noteworthily, the calculated pK_a for this site in $[NiL_2]^{-1}$ was 12.25, and this was the only site that had pK_a higher than TEA (see the Supporting Information, page 27).[46]

Further, we proceeded with the calculation for the reduction of protonated $[NiL_2]^-$ reaction intermediate, $[Ni(HL_2)]$ in two different spin states $S = 0$ or 1 with $q = 0$. For $[Ni(HL_2)]^-$, the triplet spin state was lower than the singlet by 360 kcal/mol. The second protonation on $[Ni(HL_2)]^-$ was more favorable at the N_6 nitrogen atom (Figure S35). The unavailability of labile sites on the metal in ML_2 complexes prohibits protonation on the metal. Thus, the frequently seen metal hydride intermediates in electrocatalytic HER are not suitable in this case. Rather, NiL_2 follows a ligand-centered metal-assisted pathway for catalysis. The huge intramolecular distance between the protonated sites and the unfavorability of intramolecular proton transfer from N_8 to other heteroatoms (N_4, N_2, and O_2) or the metal center suggested the need for a third protonation to initiate hydrogen generation. Among the probable protonation sites N_2, N_4, O_2, and Ni, the energetically favorable site for the third protonation was found to be N_4 (Figure S36). We also explored the possibility of intramolecular proton transfer from N_8 to N_4. However, this step was thermodynamically unfavorable, which suggests that NiL_2 follows an ECECC pathway for catalysis in the presence of TEA. Noteworthily, catalysis fails to regenerate NiL_2, rather a protonated $[Ni(HL_2)]^+$ intermediate is generated after the release of hydrogen.

2.6. Discussion. Pyridyl aroyl hydrazone ligands and their 3d transition metal complexes are relatively new to the field of electrochemical proton reduction reactions. These complexes display interesting redox behavior due to the redox non-innocence nature of the ligand. The CV of ML_2 complexes displayed metal-based $M^{III/II}$ (Fe, Co), $M^{II/I}$ (Fe, Co, Ni, Cu) redox events and a ligand-based reduction event. The ligand-based reduction is likely the electron addition to the coordinating N atom in the C=N bond, resulting in the possible formation of a ligand radical anion. The proximity of both reduction sites hints at the metal−ligand cooperativity in these complexes. Also, these complexes contain many sites in the ligand that can be protonated, making it a viable candidate for ligand-centered proton reduction reactions. From computational analysis for the Ni complex, the involvement of the ligand in catalysis was evident. All of these inferences suggest the active participation of the pyridyl aroyl hydrazone ligand in HER in its complexes. From the detailed experimental and computational analysis of the Ni complex, the role of the Ni center in catalysis was understood. It served as an auxiliary redox site, facilitating two-electron chemistry at the ligand. Such proton reduction pathways centered on ligands were less common among Ni-based complexes. We believe that for these complexes, the pathway for HER majorly depends on the pK_a of the proton source. In the present case, a weaker acid such as TEA is unable to generate a metal hydride intermediate, which is common in metal-centered HER. In stronger acids (where these complexes are stable), the HER pathway could be directed through a metal-centered pathway. The current article provides the applicability of pyridyl aroyl hydrazone ligands and their 3d transition metal complexes in electrocatalytic reduction reactions (see Figure 5).

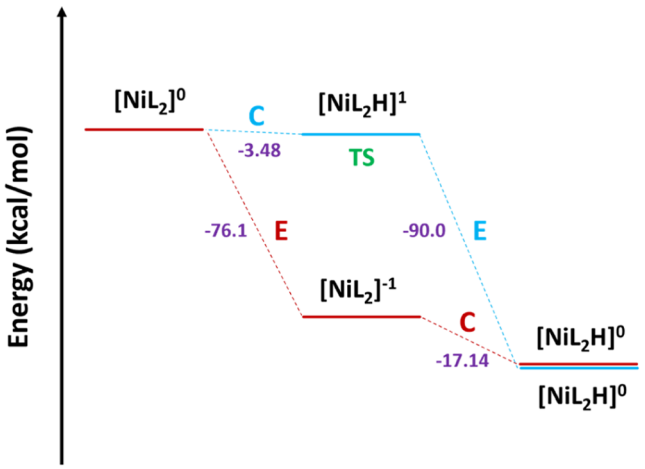

Figure 5. Energy profile diagram for the formation of $[NiL_2H]^{-1}$ through EC (red) and CE (blue) pathways (protonation at N_8). TS corresponds to the transition state.

3. CONCLUSIONS

Typically, HER catalysts operate through a metal-centered route involving a metal hydride intermediate. However, the recent decade witnessed the emergence of the best-fit HER catalyst, which follows an alternative ligand-centered pathway. In this work, we report the electrocatalytic activity of a series of pyridyl aroyl hydrazone (HL)-based metal complexes (ML_2, M = Fe, Co, Ni, Cu, and Zn) toward HER. The redox-active nature of the ligand and the availability of probable protonation sites in the ligand facilitated a ligand-centered reactivity in these complexes. We carried out a detailed mechanistic study of NiL_2 through experimental and computational analysis. Interestingly, all bond-making and -breaking reactions were centered on the ligand. We hypothesize that the lack of a vacant site in the metal complex prohibits the formation of a metal hydride intermediate, thereby driving the reaction mechanism to be mainly ligand-centered. A similar ligand-centered reactivity is expected in FeL_2, CoL_2, and CuL_2, which is yet to be confirmed.

4. EXPERIMENTAL SECTION

All starting materials and solvents were used as received unless otherwise indicated. Reagents 2-pyridine carboxaldehyde, isoniazid, iron(II) perchlorate, cobalt(II) perchlorate, cupric chloride dihydrate, nickel chloride, and zinc chloride were purchased from Sigma and TCI. Common solvents such as dichloromethane (DCM), methanol (MeOH), acetonitrile (EtCN), ethanol (EtOH), chloroform (CH_2Cl_2), tetrahydrofuran (THF), *n*-hexane, diethyl ether, and isopropanol utilized for synthesis were purchased from SRL Chemicals. HPLC-grade solvents purchased from Sigma-Aldrich were used for electrochemical studies and gas chromatography (GC) analysis.

Electrochemical studies were carried out under a nitrogen atmosphere using an AUTOLAB potentiostat PGSTAT204. Cyclic voltammetry analysis was done in a standard three-electrode cell employing a glassy carbon electrode (GCE) as the working electrode (WE), $Ag/AgNO_3$ as the reference electrode (RE), and a spiral platinum wire as the counter electrode (CE). All electrochemical studies were conducted under a nitrogen atmosphere at room temperature, and CVs are referenced against the ferrocenium/ferrocene (Fc^+/Fc)

https://doi.org/10.1021/acsomega.4c07748
ACS Omega 2025, 10, 3511−3519

couple (internal standard). Prior to each scan, glassy carbon electrodes are polished using an alumina suspension to remove any adhered substance. Reference and counter electrodes were rinsed with acetone and dimethylformamide (DMF) and dried prior to each study. Bulk electrolysis (controlled potential coulometry, CPC) experiments were conducted in a 75 mL four-neck electrolysis cell using glassy carbon plate, platinum foil, and $Ag/AgNO_3$ electrodes as working, counter, and reference electrodes, respectively.

For the detection of gases generated in the electrolysis cell, the evolved gases were subjected to GC analysis by using a thermal conductivity detector. Using a Hamilton gastight syringe, 100 μL of gas was injected into a PORA PLOT-Q column. The column was heated to 50 °C using N_2 as a carrier gas. A calibration curve was generated for the quantification of the H_2 produced. All GC analyses were carried out using an Agilent 8600 GC system equipped with a 5977B GC/MSD single quadrupole GC/MS instrument.

For the calculation of overpotential for hydrogen evolution, theoretical half-wave potential ($E^T_{1/2}$) has been calculated separately for each proton source employed using eq 1.[47]

$$E^T_{1/2} = E^0_{H^+/H_2} - 0.0591 \times pK_a + \varepsilon_D + \frac{RT}{2F}\ln\frac{C_{H_2}}{C_0} \quad (1)$$

In principle, overpotential is the additional potential required beyond the thermodynamic requirement to drive a reaction at a specific rate. Thus, it can be estimated as the difference between the theoretical half-wave potential and the experimental half-wave potential ($E_{Cat/2}$).

$$\eta = E^T_{1/2} - E_{cat/2} \quad (2)$$

Turnover number (TON) and faradaic efficiency (FE) are calculated by conducting separate CPC experiments in the presence and absence of a catalyst. CPC experiments were performed at a constant applied potential, which is equivalent to the experimental half-wave potential for each catalytic process. TON can be calculated as the ratio of experimental moles of H_2 quantified to catalyst concentration, and faradaic efficiency (FE) can be calculated from the experimental moles of H_2 and the theoretical moles of hydrogen produced, which is calculated based on the total charge passed. FE = (exp moles of H_2/theoretical mole of H_2) × 100% (see the Supporting Information for more details).

For the determination of turnover frequency (TOF), a method discussed by Artero and co-workers has been used. As the CVs reported in the current study deviate from ideal S-shape behavior, TOF cannot be calculated using the i_{cat}/i_p ratio.[38] The alternative method of wave analysis (FOWA) was not applicable in our case. Thus, CPC experiments were conducted for 3 h in the presence of 100 mM of the proton source for complexes in 0.1 M TBAF/DMF under stirring conditions. Electrode current (i_{el}) obtained from the current versus time plot from CPC is used in eq 3 to calculate TOF. Turnover frequency maximum (TOF_{max}) values were then formulated from TOF at 1.0 M acid condition.[37]

$$TOF = \frac{i_{el}^2(1 + \exp(f[E_{ap} - E_{cat/2}]))}{F^2A^2D_{cat}(C_{cat}^2)} \quad (3)$$

Chronoamperometry techniques were used to confirm the electrocatalyst transformation to a heterogenized catalytic species. In such experiments, an applied electrode potential is stepped from a voltage where no characteristic redox event of NiL_2 is present to potentials on the catalytic wave, and concurrent current responses are measured as a function of time.

UV−visible absorption spectra were recorded on an Agilent Cary 60 spectrophotometer, and FT-IR spectra were measured with an Agilent Cary 630 FT-IR equipped with an ATR spectrometer. ^{1}H NMR was recorded on a Bruker 400 MHz spectrometer, and powder X-ray diffraction data were collected using a Panalytical Empyrean Series 3 diffractometer. Mass spectrometry was done using a UHD Accurate-Mass Q-TOF LC/MS Maker-Agilent Technologies. Elemental analysis was done using a varioEL cube V4.0.11 Elementar Analysensyteme GmbH.

4.1. Computational Details. Density functional theory (DFT) was employed to carry out initial benchmark calculations using the BP86 functional using the 6-311G basis set for all of the atoms. Frequency calculations were performed in the gas phase as well as in the solution phase employing the conductor-like continuum polarizable (CPCM) model in DMF. The reduction potentials for the redox events were computed using the same level of theory and compared with the experimental data. All geometry optimization and frequency calculations were performed using ORCA-4.2.1 software, and applications such as ChemCraft and Avogadro were used for visualization and representation purposes.[44]

■ ASSOCIATED CONTENT

Supporting Information

The Supporting Information is available free of charge at https://pubs.acs.org/doi/10.1021/acsomega.4c07748.

Experimental and computational details; sample calculations; supplementary CV data; and additional spectroscopic information (PDF)

■ AUTHOR INFORMATION

Corresponding Authors

Aryya Ghosh − *Department of Chemistry, Ashoka University, Sonipat 131029 Haryana, India;* orcid.org/0000-0003-2530-234X; Email: aryya.ghosh@ashoka.edu.in

Munmun Ghosh − *Department of Chemistry, Ashoka University, Sonipat 131029 Haryana, India;* orcid.org/0000-0001-6437-6275; Email: munmun.ghosh@ashoka.edu.in

Deepak Asthana − *Department of Chemistry, Ashoka University, Sonipat 131029 Haryana, India;* orcid.org/0000-0003-1417-694X; Email: deepak.asthana@ashoka.edu.in

Authors

Bharath M − *Department of Chemistry, Ashoka University, Sonipat 131029 Haryana, India*

Gargee Roy − *Department of Chemistry, Ashoka University, Sonipat 131029 Haryana, India*

Complete contact information is available at: https://pubs.acs.org/10.1021/acsomega.4c07748

Author Contributions

†B.M. and G.R. contributed equally. Synthesis and characterization of investigated compounds were done by G.R. Electrochemical studies including HER measurements were performed by B.M. DFT calculation was performed by B.M.,

https://doi.org/10.1021/acsomega.4c07748
ACS Omega 2025, 10, 3511−3519

and A.G. D.A., and M.G. supervised the project. All authors contributed to writing the manuscript.

Funding

Startup funding was provided by Ashoka University, Sonipat, Haryana, and the Science and Engineering Research Board (SERB) startup grant (SRG/2021/001781).

Notes

The authors declare no competing financial interest.

■ ACKNOWLEDGMENTS

B.M. and G.R. are thankful to Ashoka University for their doctoral fellowship. The authors are thankful to the CRF facility, IIT Delhi (Sonipat), for their support with material characterization. M.G. acknowledges SERB, Government of India, for funding.

■ REFERENCES

(1) Zhai, W.; Ma, Y.; Chen, D.; Ho, J. C.; Dai, Z.; Qu, Y. Recent progress on the long-term stability of hydrogen evolution reaction electrocatalysts. *InfoMat* **2022**, *4* (9), No. e12357.

(2) Zeradjanin, A. R.; Grote, J.-P.; Polymeros, G.; Mayrhofer, K. J. J. A Critical Review on Hydrogen Evolution Electrocatalysis: Re-exploring the Volcano-relationship. *Electroanalysis* **2016**, *28* (10), 2256−2269.

(3) Megía, P. J.; Vizcaíno, A. J.; Calles, J. A.; Carrero, A. Hydrogen Production Technologies: From Fossil Fuels toward Renewable Sources. A Mini Review. *Energy Fuels* **2021**, *35* (20), 16403−16415.

(4) Møller, K. T.; Jensen, T. R.; Akiba, E.; Li, H.-w. Hydrogen - A sustainable energy carrier. *Prog. Nat. Sci.: Mater. Int.* **2017**, *27* (1), 34−40.

(5) Christopher, K.; Dimitrios, R. A review on exergy comparison of hydrogen production methods from renewable energy sources. *Energy Environ. Sci.* **2012**, *5* (5), 6640−6651.

(6) Howarth, R. W.; Jacobson, M. Z. How green is blue hydrogen? *Energy Sci. Eng.* **2021**, *9* (10), 1676−1687.

(7) Eftekhari, A. Electrocatalysts for hydrogen evolution reaction. *Int. J. Hydrogen Energy* **2017**, *42* (16), 11053−11077.

(8) Zhu, J.; Hu, L.; Zhao, P.; Lee, L. Y. S.; Wong, K.-Y. Recent Advances in Electrocatalytic Hydrogen Evolution Using Nanoparticles. *Chem. Rev.* **2020**, *120* (2), 851−918.

(9) Liu, F.; Shi, C.; Guo, X.; He, Z.; Pan, L.; Huang, Z.-F.; Zhang, X.; Zou, J.-J. Rational Design of Better Hydrogen Evolution Electrocatalysts for Water Splitting: A Review. *Adv. Sci.* **2022**, *9* (18), No. 2200307.

(10) Bai, S.; Yang, M.; Jiang, J.; He, X.; Zou, J.; Xiong, Z.; Liao, G.; Liu, S. Recent advances of MXenes as electrocatalysts for hydrogen evolution reaction. *npj 2D Mater. Appl.* **2021**, *5* (1), 78.

(11) Lytvynenko, A. S.; Kolotilov, S. V.; Kiskin, M. A.; Cador, O.; Golhen, S.; Aleksandrov, G. G.; Mishura, A. M.; Titov, V. E.; Ouahab, L.; Eremenko, I. L.; et al. Redox-Active Porous Coordination Polymers Prepared by Trinuclear Heterometallic Pivalate Linking with the Redox-Active Nickel(II) Complex: Synthesis, Structure, Magnetic and Redox Properties, and Electrocatalytic Activity in Organic Compound Dehalogenation in Heterogeneous Medium. *Inorg. Chem.* **2014**, *53* (10), 4970−4979.

(12) Li, C.; Baek, J.-B. Recent Advances in Noble Metal (Pt, Ru, and Ir)-Based Electrocatalysts for Efficient Hydrogen Evolution Reaction. *ACS Omega* **2020**, *5* (1), 31−40.

(13) Cai, J.; Javed, R.; Ye, D.; Zhao, H.; Zhang, J. Recent progress in noble metal nanocluster and single atom electrocatalysts for the hydrogen evolution reaction. *J. Mater. Chem. A* **2020**, *8* (43), 22467−22487.

(14) Cui, Z.; Jiao, W.; Huang, Z.; Chen, G.; Zhang, B.; Han, Y.; Huang, W. Design and Synthesis of Noble Metal-Based Alloy Electrocatalysts and Their Application in Hydrogen Evolution Reaction. *Small* **2023**, *19* (35), No. 2301465.

(15) Sarkar, S.; Peter, S. C. An overview on Pd-based electrocatalysts for the hydrogen evolution reaction. *Inorg. Chem. Front.* **2018**, *5* (9), 2060−2080.

(16) Du, P.; Eisenberg, R. Catalysts made of earth-abundant elements (Co, Ni, Fe) for water splitting: Recent progress and future challenges. *Energy Environ. Sci.* **2012**, *5* (3), 6012−6021.

(17) Song, A.; Song, S.; Duanmu, M.; Tian, H.; Liu, H.; Qin, X.; Shao, G.; Wang, G. Recent Progress of Non-Noble Metallic Heterostructures for the Electrocatalytic Hydrogen Evolution. *Small Sci.* **2023**, *3* (9), No. 2300036.

(18) Zheng, Y.; Jiao, Y.; Zhu, Y.; Li, L. H.; Han, Y.; Chen, Y.; Du, A.; Jaroniec, M.; Qiao, S. Z. Hydrogen evolution by a metal-free electrocatalyst. *Nat. Commun.* **2014**, *5* (1), No. 3783.

(19) McCool, J. D.; Zhang, S.; Cheng, I.; Zhao, X. Rational development of molecular earth-abundant metal complexes for electrocatalytic hydrogen production. *Chin. J. Catal.* **2022**, *43* (12), 3019−3045.

(20) Wang, M.; Chen, L.; Sun, L. Recent progress in electrochemical hydrogen production with earth-abundant metal complexes as catalysts. *Energy Environ. Sci.* **2012**, *5* (5), 6763−6778.

(21) McKone, J. R.; Marinescu, S. C.; Brunschwig, B. S.; Winkler, J. R.; Gray, H. B. Earth-abundant hydrogen evolution electrocatalysts. *Chem. Sci.* **2014**, *5* (3), 865−878.

(22) Thoi, V. S.; Sun, Y.; Long, J. R.; Chang, C. J. Complexes of earth-abundant metals for catalytic electrochemical hydrogen generation under aqueous conditions. *Chem. Soc. Rev.* **2013**, *42* (6), 2388−2400.

(23) Li, A.; Sun, Y.; Yao, T.; Han, H. Earth-Abundant Transition-Metal-Based Electrocatalysts for Water Electrolysis to Produce Renewable Hydrogen. *Chem. − Eur. J.* **2018**, *24* (69), 18334−18355.

(24) Phipps, C. A.; Hofsommer, D. T.; Toda, M. J.; Nkurunziza, F.; Shah, B.; Spurgeon, J. M.; Kozlowski, P. M.; Buchanan, R. M.; Grapperhaus, C. A. Ligand-Centered Hydrogen Evolution with Ni(II) and Pd(II)DMTH. *Inorg. Chem.* **2022**, *61* (25), 9792−9800.

(25) Razavet, M.; Artero, V.; Fontecave, M. Proton Electroreduction Catalyzed by Cobaloximes: Functional Models for Hydrogenases. *Inorg. Chem.* **2005**, *44* (13), 4786−4795.

(26) Helm, M. L.; Stewart, M. P.; Bullock, R. M.; DuBois, M. R.; DuBois, D. L. A Synthetic Nickel Electrocatalyst with a Turnover Frequency Above 100,000 s^{-1} for H_2 Production. *Science* **2011**, *333* (6044), 863−866.

(27) Bhugun, I.; Lexa, D.; Savéant, J.-M. Homogeneous Catalysis of Electrochemical Hydrogen Evolution by Iron(0) Porphyrins. *J. Am. Chem. Soc.* **1996**, *118* (16), 3982−3983.

(28) Barrozo, A.; Orio, M. Molecular Electrocatalysts for the Hydrogen Evolution Reaction: Input from Quantum Chemistry. *ChemSusChem* **2019**, *12* (22), 4905−4915.

(29) Haddad, A. Z.; Kumar, D.; Ouch Sampson, K.; Matzner, A. M.; Mashuta, M. S.; Grapperhaus, C. A. Proposed Ligand-Centered Electrocatalytic Hydrogen Evolution and Hydrogen Oxidation at a Noninnocent Mononuclear Metal−Thiolate. *J. Am. Chem. Soc.* **2015**, *137* (29), 9238−9241.

(30) Haddad, A. Z.; Cronin, S. P.; Mashuta, M. S.; Buchanan, R. M.; Grapperhaus, C. A. Metal-Assisted Ligand-Centered Electrocatalytic Hydrogen Evolution upon Reduction of a Bis(thiosemicarbazonato)-Cu(II) Complex. *Inorg. Chem.* **2017**, *56* (18), 11254−11265.

(31) Cronin, S. P.; Mamun, A. A.; Toda, M. J.; Mashuta, M. S.; Losovyj, Y.; Kozlowski, P. M.; Buchanan, R. M.; Grapperhaus, C. A. Utilizing Charge Effects and Minimizing Intramolecular Proton Rearrangement to Improve the Overpotential of a Thiosemicarbazonato Zinc HER Catalyst. *Inorg. Chem.* **2019**, *58* (19), 12986−12997.

(32) Wicker, S. A.; Hutchison, P.; Musicante, R. G.; Kiker, M. T.; Suffern, N. C.; Graham, D. K.; Rhodes, L. M.; Binu, A. P.; Jean-Francois, S. A.; Graves, A. S.; et al. Hydrogen Production Using a Nickel Catalyst Combining Redox Activity and Pendent Base Effects. *Inorg. Chem.* **2024**, *63* (1), 451−461.

(33) Jain, R.; Mamun, A. A.; Buchanan, R. M.; Kozlowski, P. M.; Grapperhaus, C. A. Ligand-Assisted Metal-Centered Electrocatalytic

https://doi.org/10.1021/acsomega.4c07748
ACS Omega 2025, 10, 3511−3519

Hydrogen Evolution upon Reduction of a Bis(thiosemicarbazonato)-Ni(II) Complex. *Inorg. Chem.* **2018**, *57* (21), 13486−13493.
(34) Haddad, A. Z.; Garabato, B. D.; Kozlowski, P. M.; Buchanan, R. M.; Grapperhaus, C. A. Beyond Metal-Hydrides: Non-Transition-Metal and Metal-Free Ligand-Centered Electrocatalytic Hydrogen Evolution and Hydrogen Oxidation. *J. Am. Chem. Soc.* **2016**, *138* (25), 7844−7847.
(35) Armstrong, C. M.; Bernhardt, P. V.; Chin, P.; Richardson, D. R. Structural Variations and Formation Constants of First-Row Transition Metal Complexes of Biologically Active Aroylhydrazones. *Eur. J. Inorg. Chem.* **2003**, *2003* (6), 1145−1156.
(36) Lytvynenko, A. S.; Mishura, A. M.; Titov, V. E.; Kiskin, M. A.; Golhen, S.; Cador, O.; Kolotilov, S. V.; Ouahab, L.; Eremenko, I. L.; Novotortsev, V. M. Structure, magnetic, and electrochemical properties of complexes of 3d-metals as redox-active units for assembling coordination polymers and porous coordination polymer on their basis. *Russ. Chem. Bull.* **2015**, *64* (2), 306−317.
(37) Queyriaux, N.; Sun, D.; Fize, J.; Pécaut, J.; Field, M. J.; Chavarot-Kerlidou, M.; Artero, V. Electrocatalytic Hydrogen Evolution with a Cobalt Complex Bearing Pendant Proton Relays: Acid Strength and Applied Potential Govern Mechanism and Stability. *J. Am. Chem. Soc.* **2020**, *142* (1), 274−282.
(38) Rountree, E. S.; McCarthy, B. D.; Eisenhart, T. T.; Dempsey, J. L. Evaluation of Homogeneous Electrocatalysts by Cyclic Voltammetry. *Inorg. Chem.* **2014**, *53* (19), 9983−10002.
(39) Li, C.-B.; Bagnall, A. J.; Sun, D.; Rendon, J.; Koepf, M.; Gambarelli, S.; Mouesca, J.-M.; Chavarot-Kerlidou, M.; Artero, V. Electrocatalytic reduction of protons to dihydrogen by the cobalt tetraazamacrocyclic complex [Co(N4H)Cl2]+: mechanism and benchmarking of performances. *Sustainable Energy Fuels* **2021**, *6* (1), 143−149.
(40) Straistari, T.; Fize, J.; Shova, S.; Réglier, M.; Artero, V.; Orio, M. A Thiosemicarbazone−Nickel(II) Complex as Efficient Electrocatalyst for Hydrogen Evolution. *ChemCatChem* **2017**, *9* (12), 2262−2268.
(41) Lee, K. J.; McCarthy, B. D.; Dempsey, J. L. On decomposition, degradation, and voltammetric deviation: the electrochemist's field guide to identifying precatalyst transformation. *Chem. Soc. Rev.* **2019**, *48* (11), 2927−2945.
(42) Lee, K. J.; McCarthy, B. D.; Rountree, E. S.; Dempsey, J. L. Identification of an electrode-adsorbed intermediate in the catalytic hydrogen evolution mechanism of a cobalt dithiolene complex. *Inorg. Chem.* **2017**, *56* (4), 1988−1998.
(43) Sun, D.; Harshan, A. K.; Pécaut, J.; Hammes-Schiffer, S.; Costentin, C.; Artero, V. Hydrogen Evolution Mediated by Cobalt Diimine-Dioxime Complexes: Insights into the Role of the Ligand Acid/Base Functionalities. *ChemElectroChem* **2021**, *8* (14), 2671−2679.
(44) Neese, F. Software update: The ORCA program system—Version 5.0. *WIREs Comput. Mol. Sci.* **2022**, *12* (5), No. e1606.
(45) Cossi, M.; Rega, N.; Scalmani, G.; Barone, V. Energies, structures, and electronic properties of molecules in solution with the C-PCM solvation model. *J. Comput. Chem.* **2003**, *24* (6), 669−681.
(46) Solis, B. H.; Hammes-Schiffer, S. Proton-Coupled Electron Transfer in Molecular Electrocatalysis: Theoretical Methods and Design Principles. *Inorg. Chem.* **2014**, *53* (13), 6427−6443.
(47) Fourmond, V.; Jacques, P.-A.; Fontecave, M.; Artero, V. H2 Evolution and Molecular Electrocatalysts: Determination of Overpotentials and Effect of Homoconjugation. *Inorg. Chem.* **2010**, *49* (22), 10338−10347.

https://doi.org/10.1021/acsomega.4c07748
ACS Omega 2025, 10, 3511−3519